Gauge cell method for simulation studies of phase transitions in confined systems

Alexander V. Neimark* and Aleksey Vishnyakov
TRI/Princeton, 601 Prospect Avenue, Princeton, New Jersey 08542
(Received 20 March 2000)

A method for Monte Carlo studies of phase equilibrium in confined systems is presented using an example of vapor-liquid equilibrium (capillary condensation and evaporation) in cylindrical pores. The method, named the gauge cell method, allows one to construct the full phase diagram of a confined fluid in the form of a van der Waals loop, which includes stable, metastable, and unstable equilibrium states. The phase coexistence is then determined by thermodynamic integration along the metastable and unstable regions of the phase diagram employing Maxwell's rule of equal areas. The simulation results agree with experimental data on the capillary condensation of nitrogen at its boiling temperature on mesoporous molecular sieves. The method can be applied to other phase transitions in confined systems such as fluid-fluid separation, layering, and freezing.

PACS number(s): 02.50.Ng, 64.70.Fx, 68.45.Da, 02.70.Lq

I. INTRODUCTION

A great deal of work has been done on the molecular modeling of phase equilibrium in confining geometries, primarily on studies of adsorption and capillary condensation of simple fluids in pores of a few molecular diameters in width; for the most recent review see [1]. The structure and properties of fluids confined within nanopores differ significantly from those of bulk fluids. Interactions with solid walls and geometrical restrictions on possible fluctuations cause shifts in phase transitions and critical points compared with the bulk, multiplicity of observable metastable states, and associated hysteresis. These phenomena are well documented on silica gels, porous glasses, carbons, and other nanoporous solids [2]. Recent intense studies of capillary condensation in cylindrical pores of mesoporous molecular sieves of MCM-41 type provided theoreticians with reliable experimental data in a wide range of temperatures and pore sizes [3–7]. Molecular modeling, mainly grand canonical Monte Carlo (GCMC) simulations, has been proved the most efficient tool for the modeling of vapor-liquid equilibrium in pores of various shapes and is successfully employed by a number of researchers to explain the specifics of capillary condensation in nanoporous materials [8–17]. At subcritical conditions, GCMC simulations allow one to construct the hysteresis loop formed by discontinuous adsorption and desorption isotherms and vertical steps corresponding to spontaneous condensation and evaporation but are not capable of determining the equilibrium transition between vaporlike and liquidlike states. Several special methods were developed to find the conditions of the phase coexistence in pores by means of molecular simulations (e.g., [18–22]). These methods require additional simulations and are sometimes difficult to implement.

In this paper, we present a method for determining the equilibrium transition and also the true limits of stability (spinodals) of the vaporlike and liquidlike metastable states. The method is based on the construction of the continuous adsorption isotherm in the form of a van der Waals loop, which includes stable, metastable, and unstable equilibrium states, and thermodynamic integration along the metastable and unstable regions of the isotherm, employing Maxwell's rule of equal areas. In so doing, the energy barrier separating the metastable and stable states and, correspondingly, the probability of spontaneous capillary condensation and evaporation can be also determined. The simulation results are shown to agree with experimental data on the capillary condensation of nitrogen at its boiling temperature on mesoporous molecular sieves. The method proposed provides useful insight into the origin of capillary hysteresis, inherent in nanoporous materials, and can also be applied to other phase transitions in confined systems, such as fluid-fluid separation, layering, and freezing. In subsequent sections we present a brief review of the simulation methods of phase equilibrium of a simple fluid in confining geometry (Sec. II), introduce the gauge cell method (Sec. III), and present examples of simulation results on the capillary condensation of nitrogen in silica nanopores (Sec. IV). We also compare our results with other simulation methods (Sec. V and VI) and experimental data on MCM-41 materials (Sec. VII).

II. MC METHODS FOR STUDYING PHASE EQUILIBRIUM IN A CONFINING GEOMETRY

In GCMC simulations, one generates equilibrium states at a given temperature T and chemical potential μ which correspond to equilibrium with an infinite bulk fluid reservoir. The simulation cell represents a pore space available for the fluid molecules, which experience the external potential $\Phi_{ext}(r)$ exerted by the pore walls. The pore geometry, its volume V, and surface A are fixed. At these conditions, the equilibrium states correspond to minima of the grand thermodynamic potential $\Omega(T,\mu)$ given by

$$\Omega = F - \mu N, \tag{1}$$

where F is the Helmholtz free energy and N is the number of molecules in the cell. Because the pore geometry is assumed to be unchanged, the fundamental equation for the grand thermodynamic potential of a confined fluid is given by

$$d\Omega = -S\,dT - N\,d\mu, \tag{2}$$

*Email address: aneimark@triprinceton.org

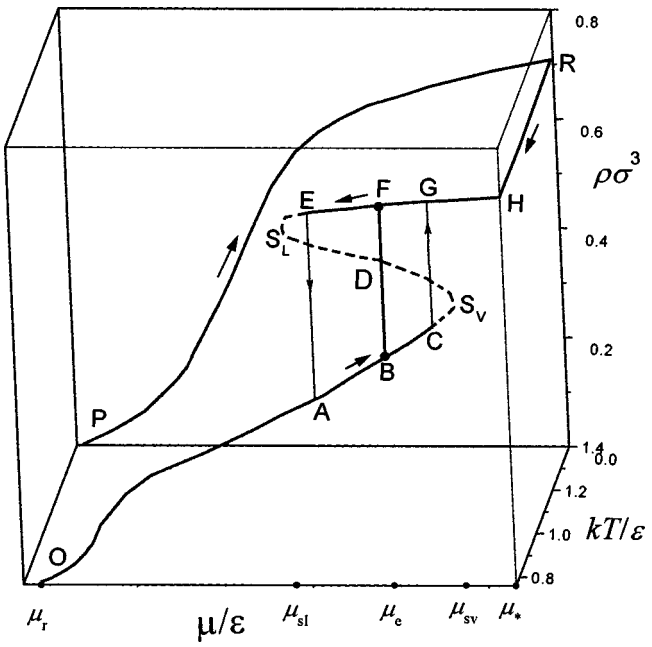

FIG. 1. Three-dimensional sketch describing the gauge cell method. Subcritical adsorption isotherm OH ($kT/\epsilon=0.762$) is shown in the front face. O, initial ideal vaporlike state: B, vaporlike state at vapor-liquid coexistence: C, limit of stability of the vaporlike phase in the GCMC method (the fluid undergoes a spontaneous transition to point G): S_v, vaporlike spinodal: D, unstable state at $\mu=\mu_e$: S_l, liquidlike spinodal: E, limit of stability of the liquidlike phase in the GCMC method (the fluid undergoes a spontaneous transition to point A): F, liquidlike state at the vapor-liquid coexistence: H, stable liquidlike state at $\mu=\mu_*$. Solid bold lines show stable and metastable states, which are achieved in GCMC simulations. The dashed line represents metastable (CS_v and S_lE) and unstable (S_vDS_l) states, which are achieved in the pore-gauge GEMC simulations. The supercritical isotherm PR ($kT/\epsilon=1.379$) and a path of constant chemical potential RH ($\mu=\mu_*$), which are used in the PG method of thermodynamic integration, are shown in the back face and in the right side face, respectively. P, ideal vaporlike state: R, dense fluid state at $\mu=\mu_*$. The vertical line BF shows the vapor-liquid coexistence. The Maxwell rule implies that area $BS_vDB=$ area FDS_lF.

where S is the entropy. The adsorption isotherm $N(\mu)_T$ satisfies the Gibbs adsorption equation given by

$$N=-(\partial\Omega/\partial\mu)_T. \tag{3}$$

A typical adsorption-desorption isotherm generated by GCMC is schematically presented in Fig. 1 (line *OABC-DEFGH*). The adsorption is expressed as the average fluid density $\rho=N/V$. The adsorption branch terminates at point C, where the limit of stability of the vaporlike states was achieved in the simulation and the system spontaneously jumped into a liquidlike state, point G. This transition corresponds to spontaneous condensation. The desorption branch terminates at point E, where the limit of stability of the liquidlike states was achieved and the system spontaneously jumped into a vaporlike state, point A. This transition corresponds to spontaneous evaporation. Points C and E are close to, yet do not necessarily coincide, with the true limits of stability or the vaporlike and liquidlike spinodals of the theoretical phase diagram, S_v and S_l. Capillary hysteresis is observed in the region where the grand thermodynamic potential has at least two minima separated by energetic barrier which the system cannot overcome due to the inherent restrictions imposed on possible fluctuations.

The true phase equilibrium achieved somewhere between the spinodals is determined from the equality of the grand thermodynamic potentials in the coexisting vaporlike and liquidlike states on the adsorption and desorption branches, respectively:

$$\Omega_a(\mu_e)=\Omega_d(\mu_e). \tag{4}$$

The bulk pressure corresponding to the equilibrium in the pore is obtained from the bulk equation of state, such as the equation of Johnson *et al.* [23] in the case of a Lennard-Jones (LJ) fluid. Because the GCMC simulation does not allow one to calculate the grand thermodynamic potential directly, it can be obtained by thermodynamic integration. Along the adsorption branch, $\Omega(\mu)$ is easily calculated by integrating the Gibbs equation (3) from a reference state of which the grand thermodynamic potential is known. Choosing the reference state at a sufficiently small chemical potential μ_r to provide the fluid ideality (point O in Fig. 1), one obtains:

$$\begin{aligned}\Omega_a(\mu,T)&=\Omega_r(\mu,T)-\int_{\mu_r}^{\mu}N_a(\mu,T)d\mu\\&=-kTN_a(\mu_r,T)-\int_{\mu_r}^{\mu}N_a(\mu,T)d\mu.\end{aligned} \tag{5}$$

Integration in Eq. (5) can be accomplished along the reversible part of the adsorption isotherm up to the stability limit, point C, where spontaneous condensation was observed.

To calculate the grand thermodynamic potential along the desorption branch of the isotherm, one has to construct a continuous reversible trajectory of equilibrium states, circumventing the hysteresis region, which connects a liquidlike state on the desorption isotherm with a reference state whose grand thermodynamic potential is known. Peterson and Gubbins [18] suggested to construct a trajectory composed of two parts, a reversible supercritical isotherm $N(\mu,T_s)$, $T_s>T_c$ (line PR in Fig. 1) and a path of constant chemical potential $N(\mu_*,T)$; $\mu_*>\mu_{sl}$ (line RH in Fig. 1). In so doing, the grand thermodynamic potential for a liquidlike state on the desorption isotherm is given by

$$\begin{aligned}\Omega_d(\mu,T)=kTN(\mu_{rs},T_s)&-\int_{\mu_r}^{\mu_*}N(\mu,T_s)d\mu\\&-T\int_{1/T_s}^{1/T}(U(\mu_*,T)-\mu_*N)d(1/T)\\&-\int_{\mu_*}^{\mu_r}N(\mu,T)d\mu.\end{aligned} \tag{6}$$

Here, U is the total internal energy given by $\langle E\rangle+(3/2)NkT$: $\langle E\rangle$ is the average potential energy directly calculated in the GCMC simulation. The Peterson-Gubbins (PG) method was used for the determination of the phase

coexistence in pores [8,11,12,15]. This method, although theoretically irreproachable, requires additional intense simulations, and inevitable errors of integration may lead to an appreciable inaccuracy in the estimation of μ_e. The uncertainty is mostly associated with integration along the path *RH* of equal chemical potential [the second integral on the right side of Eq. (6)]. Detailed examples are presented below in Sec. V.

Panagiotopoulos [21,22] proposed the Gibbs ensemble Monte Carlo (GEMC) method to determine phase equilibria in the bulk and confinement. As applied to phase coexistence in pores, the GEMC method implies simulation of two phases in two simulation cells, which represent two similar pores, allowing for both mass and volume exchange between the cells. In so doing, the pore-pore GEMC method directly gives the densities (and/or compositions) of the coexisting phases. However, it does not specify the equilibrium chemical potential μ_e at which phase coexistence occurs. The equilibrium chemical potential μ_e can be estimated by either using the Widom method [24] [e.g., Smit [25] applied this technique to determine $\mu_e(T)$ for the bulk LJ fluid] or interpolating the equilibrium density obtained by the pore-pore GEMC simulation onto the corresponding branch of the GCMC isotherm. Instead of the GCMC method, the adsorption and desorption isotherms can be determined by the pore-fluid GEMC method [22]. This approach was used by Lastoskie *et al.* [26] to determine the conditions of the vapor-liquid equilibrium in carbon slit-shaped pores. The pore-pore GEMC method was employed for studies of capillary condensation and liquid-liquid equilibria [22,26–28]. In our experience, when the pore-pore GEMC method is applied to the capillary condensation coexistence in the nanopores with strongly attractive walls, which cause the existence of a dense monolayer, and, correspondingly, a small compressibility of the liquidlike phase, the coexistence point determined after a reasonable number of configurations (ca. 3×10^7) is sensitive to the initial configuration. Examples are presented below in Sec. VI. Other simulation methods applied to studying the phase equilibrium, such as the methods of histogram reweighting [29–31] and the Gibbs-Duhem integration method [32], have not yet been implemented to study capillary condensation phenomena.

III. GAUGE CELL METHOD

The proposed method is based on thermodynamic integration. Instead of constructing additional equilibrium states at elevated temperatures, as required by the PG method, we propose to connect the vaporlike and liquidlike spinodals by a continuous path of equilibrium, yet unstable, states and then to determine the phase coexistence from the Maxwell rule of equal areas (see the dotted trajectory S_vDS_l). This procedure is proved legitimate for bulk phase equilibrium (e.g., [33]). Qualitatively, use of the van der Waals–type isotherms for interpreting the capillary condensation was discussed earlier (see, e.g., [34–36]). A physically unstable state can be stabilized in simulations when the density fluctuations are severely suppressed. The possibility to extend the sorption isotherm to the unstable region was shown previously for lattice models [37,38], canonical ensemble molecular dynamics [39], canonical and Gibbs ensemble MC simulations [40], and canonical ensemble density functional theory [41].

A. Pore-gauge GEMC simulation

To construct the continuous trajectory of states with the average density $N_u(\mu,T)$ between the densities of the vaporlike and liquidlike spinodals, we render the GEMC simulation in two cells which are in thermal equilibrium with an infinite heat bath. One of the cells represents the pore and the other is a gauge cell of a limited capacity. The phase diagram for the gauge cell is determined independently and assumed to be known. Thus, the fluid in the gauge cell serves as a reference. The Gibbs ensemble under consideration is the canonical ensemble for the total system of two simulation cells. We allow mass exchange between the cells; however, the cell volumes are kept unchanged. Thus, we do not require mechanical equilibrium between the confined fluid and the reference, similar to the pore-fluid GEMC method [22,42]. Therefore, the conditions of isothermal equilibrium come to the equality of the chemical potentials in the confined and reference fluids.

The limited capacity of the reference cell constrains density fluctuations in the confined fluid and allows the confined fluid to be kept in a state which would be unstable in contact with the bulk. Indeed, the Gibbs ensemble implies the minimization of the total Helmholtz free energy in two cells,

$$F(N,V,T)+F_g(N_g,V_g,T)\rightarrow\min, \tag{7}$$

at the conditions

$$N_\Sigma=N+N_g=\text{const}, \quad V,V_g,T=\text{const}. \tag{8}$$

Here and below, extensive quantities without a subscript are referred to the pore cell, and quantities with the subscript ''g'' are referred to the gauge cell. The condition (7) of the total Helmholtz free energy minimum leads to the equilibrium condition, given by

$$\mu=(\partial F/\partial N)|_{V,T}=(\partial F_g/\partial N_g)|_{V_g,T} \tag{9}$$

and the stability condition for the total system given by

$$(\partial^2F/\partial N^2)|_{V,T}+(\partial^2F_g/\partial N_g^2)|_{V_g,T}>0. \tag{10}$$

Note that inequality (10) does not require the fulfillment of the conditions of thermodynamic stability in each of the cells separately. It is assumed that at the conditions of simulations the reference fluid in the gauge cell is stable: i.e., its isothermal compressibility is positive and

$$\left.\frac{\partial^2F_g}{\partial N_g^2}\right|_{V_g,T}=\frac{1}{V_g}\left.\frac{\partial\mu}{\partial\rho_g}\right|_T>0. \tag{11}$$

However, it is not required for the confined fluid to be stable.

To study unstable states with a negative compressibility $(\partial^2F/\partial N^2)|_{V,T}<0$, one has to choose a gauge cell with a sufficiently small volume. Namely, the ratio of the pore and gauge volumes V_g/V must satisfy the inequality

$$\frac{1}{V_g}\frac{\partial\mu}{\partial\rho_g}\bigg|_T+\frac{1}{V}\frac{\partial\mu}{\partial\rho}\bigg|_T>0 \quad \text{or} \quad V_g\frac{\partial\rho_g}{\partial\mu}<V\left|\frac{\partial\rho}{\partial\mu}\right|$$

$$\text{or} \quad \frac{V_g}{V}<\left|\frac{\partial\rho}{\partial\mu}\right| \Big/ \frac{\partial\rho_g}{\partial\mu}. \tag{12}$$

The gauge cell (its geometry, boundary conditions, and external potentials, if any) can be chosen for reasons of convenience. When the reference fluid in the gauge cell behaves as an ideal gas, condition (12) reduces to

$$\frac{V_g}{V}<\left|\frac{\partial\rho}{\partial\mu}\right| \Big/ \frac{\rho_g}{kT}. \tag{13}$$

The possibility of observations of unstable states in adsorption experiments with a limited vapor volume was discussed by Everett [43].

The pore-gauge GEMC simulations with a suitably chosen gauge cell volume enable one to generate stable and metastable adsorption and desorption states extended up to the true limits of stability of the vaporlike and liquidlike states and also the backward trajectory of unstable states $N_u(\mu)$ which connects the vaporlike and liquidlike spinodals (see the dotted line CS_vDS_lE in Fig. 1). In the region of applicability of the GCMC method, the states generated by both methods coincide. Here, we do not consider extremely small confinements containing only a few molecules, in which the results obtained in the grand canonical and canonical ensembles may differ [44].

Inequality (13) bounds the conditions at which the backward trajectory S_vDS_l of the unstable states can be generated in pore-gauge GEMC simulations. In general, we do not exclude that while constructing the unstable states starting from the spinodal S_v or S_l one may arrive at a state of zero compressibility, $\partial\rho/\partial\mu=0$. This state cannot be stabilized by external forces and would not be achievable in simulations. Although we did not meet the states of zero compressibility in the simulations presented below, their existence for particular types of fluid-solid interactions is, in principle, possible. Paraphrasing the definition of the spinodal as the true limit of stability of metastable states, the state of zero compressibility can be referred to as the true limit of stabilization of unstable states or superspinodal.

The systems exhibiting the superspinodal may feature intriguing behaviors [45]. Thus, provided inequality (13) is satisfied, one can construct the continuous S-shaped trajectory of the equilibrium states similar to the van der Waals loop.

B. Condition of phase coexistence

In the unstable states on the backward trajectory of the constructed S-shaped adsorption isotherm, the grand thermodynamic potential defined by Eq. (1) can be determined by the integration of the Gibbs equation (3). Thus, the difference between the grand thermodynamic potential in the vaporlike (μ_{sv}) and liquidlike spinodals (μ_{sl}), which spans the gap between the adsorption and desorption isotherms, is given by

$$\Omega_d(\mu_{s1},T)-\Omega_a(\mu_{sv},T)=-\int_{\mu_{sv}}^{\mu_{sl}}N_u(\mu,T)d\mu$$

$$=+\int_{\mu_{sl}}^{\mu_{sv}}N_u(\mu,T)d\mu. \tag{14}$$

And the grand thermodynamic potential along the desorption branch is calculated as

$$\Omega_d(\mu,T)=\Omega_a(\mu_{sv},T)+\int_{\mu_{sl}}^{\mu_{sv}}N_u(\mu,T)d\mu$$

$$-\int_{\mu_{sl}}^{\mu}N_d(\mu,T)d\mu. \tag{15}$$

In so doing, the condition (4) of phase coexistence comes to the Maxwell rule of equal areas:

$$\int_{\mu_e}^{\mu_{sv}}N_a(\mu,T)d\mu-\int_{\mu_{sl}}^{\mu_{sv}}N_u(\mu,T)d\mu+\int_{\mu_e}^{\mu_{sl}}N_d(\mu,T)d\mu=0. \tag{16}$$

It is worth noting that, in principle, instead of employing the gauge cell to measure the chemical potential, one can generate the backward trajectory by the canonical ensemble simulation [40]. However, in this case the chemical potential has to be determined by the Widom method [24], which, in our experience, is less accurate than the gauge cell method.

C. Energy barriers for spontaneous capillary condensation and evaporation

In the hysteresis region, the transition from a metastable state to a stable state is associated with an energy barrier. When the energy barrier can be overcome by density fluctuations in the pore, this transition occurs spontaneously. In the pore-gauge GEMC simulations, the density fluctuations are suppressed and spontaneous transitions are not observed. In the GCMC simulations, one may expect that the probability of the spontaneous transition depends on the height of the energy barrier. The height of the energy barrier is determined by the grand potential in the saddle points, which correspond to the backward trajectory of the phase diagram. At a given chemical potential μ the energy barrier is proportional to the difference of the grand potentials in the unstable state on the backward trajectory and in the metastable state:

$$\Omega_*(\mu)=\Omega_u(\mu)-\Omega_a(\mu), \quad \mu>\mu_e \ \text{(condensation)},$$

$$\Omega_*(\mu)=\Omega_\mu(\mu)-\Omega_d(\mu),$$

$$\mu<\mu_e \ \text{(evaporation)}. \tag{17}$$

The potential barrier (17) vanishes at the spinodals and achieves a maximum at the equilibrium. For the case of cylindrical pores considered in our simulations, it is convenient to operate with the potential barrier $\tilde{\Omega}_*(\mu)$ reduced per unit of pore length. In so doing, the probability of the spontaneous transition is proportional to the Arrhenius factor given by

$$P_*(\mu)=\exp[-l\Delta\tilde{\Omega}_*(\mu)/kT]. \tag{18}$$

Here, l is a characteristic length which depends on the linear scale of the developing fluctuation. Physically, this fluctuation in the process of condensation can be imagined as a film undulation transforming into a liquid bridge which spans the pore. The process of spontaneous evaporation (desorption) starts from the coalescence of intermolecular cavities into a ''bubble,'' the linear scale of such fluctuations of density of the order of the pore width. Thus, in the estimates presented below, the characteristic scale in the Arrhenius factor (18) is assumed to be equal to the pore width. While analyzing phase transitions in other confining geometries, the potential barrier should be reduced for reasons of convenience; for example, in a slit-shaped geometry, it seems reasonable to use the potential barrier reduced per unit of pore surface area.

The possibility to analyze the potential barriers and the probability of spontaneous transitions is an additional advantage of the proposed gauge cell method. This constitutes a basis for formulations of the conditions of reversibility of simulated and experimental adsorption isotherms.

IV. SIMULATION RESULTS

We applied the gauge cell method to study the vapor-liquid coexistence of a LJ fluid in two cylindrical pores of 13σ and 10σ in width at the reduced temperature $kT/\epsilon = 0.762$ (σ and ϵ denote geometric and energetic LJ parameters for the fluid molecule). We constructed stable and unstable adsorption isotherms using the GCMC and the pore-gauge GEMC simulations and determined the conditions of the two-phase coexistence by the Maxwell rule of equal areas. The results were compared with the estimates obtained using the PG [18] and pore-pore GEMC methods [22], and also with the experimental data on the nitrogen capillary condensation on MCM-41 materials.

A. Pore model and simulation details

In our simulations, the LJ potential was cut at 5σ and shifted. Solid-fluid interactions were modeled as the LJ interaction of a fluid molecule with a single structureless cylindrical layer of atoms composing the pore wall [3]:

$$\Phi_{\mathrm{ext}}(r,R) = \pi^2 \rho_s \epsilon_{sf} \sigma_{sf}^2 \left\{ \frac{63}{32} \left[\frac{r}{\sigma_{sf}} \left(2 - \frac{r}{R} \right) \right]^{-10} \times F\left[-\frac{9}{2}; -\frac{9}{2}; 1; \left(1 - \frac{r}{R} \right)^2 \right] - 3 \left[\frac{r}{\sigma_{sf}} \left(2 - \frac{r}{R} \right) \right]^{-4} \times F\left[-\frac{3}{2}; -\frac{3}{2}; 1; \left(1 - \frac{r}{R} \right)^2 \right] \right\}. \quad (19)$$

Here $R = H/2$ is the pore radius, measured to the center of the first layer of solid atoms in the pore wall, r is the distance from adsorbate molecule to the wall, ρ_s is the surface number density of LJ atoms in the pore wall, and $F[\alpha;\beta;\gamma;\delta]$ is the hypergeometric series. The fluid-fluid and solid-fluid parameters were chosen to represent nitrogen in silica pores of MCM-41: $\sigma = 3.6154$ Å, $\epsilon/k = 101.5$ K [46], $\sigma_{sf} = 3.17$ Å, and $\rho_s \epsilon_{sf}/k = 2253$ K [4]. A reduced temperature of $kT/\epsilon = 0.762$ corresponds to 77.4 K, which is the experimental boiling temperature of nitrogen at $p = 1$ atm.

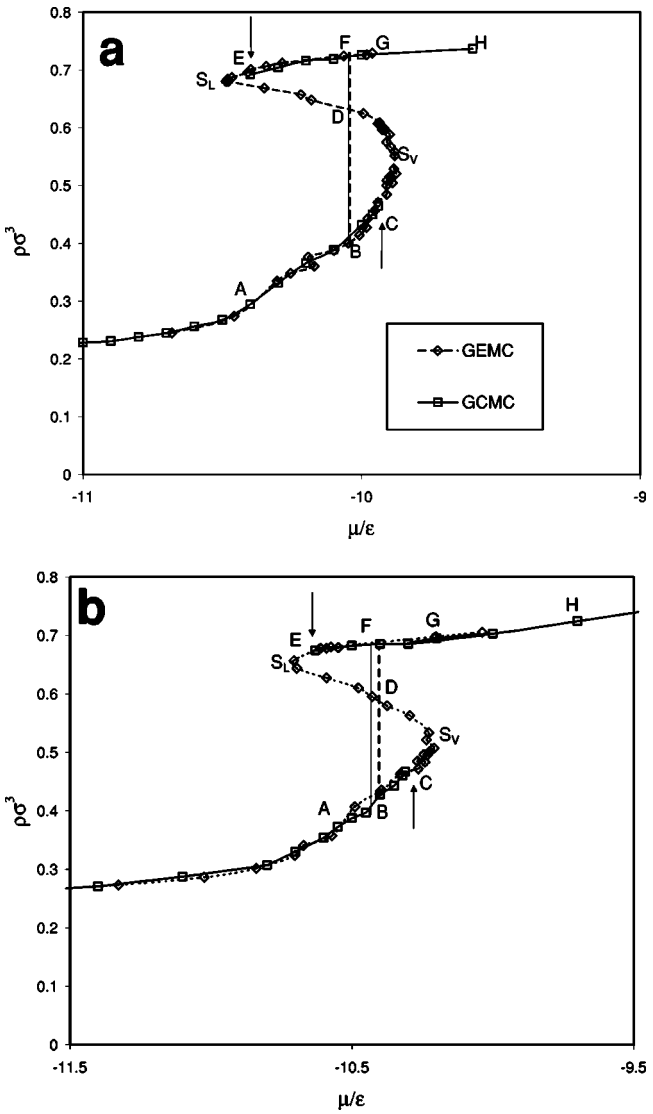

FIG. 2. Pore-gauge GEMC and GCMC isotherms of nitrogen adsorption at $kT/\epsilon = 0.762$ (77.4 K) in cylindrical 13σ (a) and 10σ (b) pores. Denotations correspond to Fig. 1. Vertical lines show the location of vapor-liquid coexistence calculated by the gauge cell method (bold dashed line) and PG method (thin solid line, average of the calculations with $\mu_* = -10.0$, -9.7, and -9.4ϵ). Arrows (C and E) indicate the stability limits in GCMC simulations.

In the pore cell, the periodic boundary conditions were applied in the z direction parallel to the pore walls. The pore length was 10σ. As the gauge cell, a cube with triply periodic boundary conditions was employed. The size of the gauge cell varied from 30σ to 50σ and was adjusted so that a sufficient number of fluid molecules (ca. 30) were contained in the gauge cell in each simulation. The gauge cell was calibrated by a series of GCMC simulations of the same length as that of the pore simulations. Even for the smallest bulk cell length 30σ, the fluid in the gauge cell behaved as an ideal bulk vapor; no notable nonideality of the gauge fluid was observed at $\mu < -9.6\epsilon$ and $kT/\epsilon = 0.762$. Note that according to the equation of Johnson *et al.* [23], the vapor-liquid equilibrium in the bulk LJ fluid at $kT/\epsilon = 0.762$ corresponds to $\mu_0 = -9.34\epsilon$.

A typical simulation run consisted of 3×10^4 steps per molecule in the pore cell: the average properties were calcu-

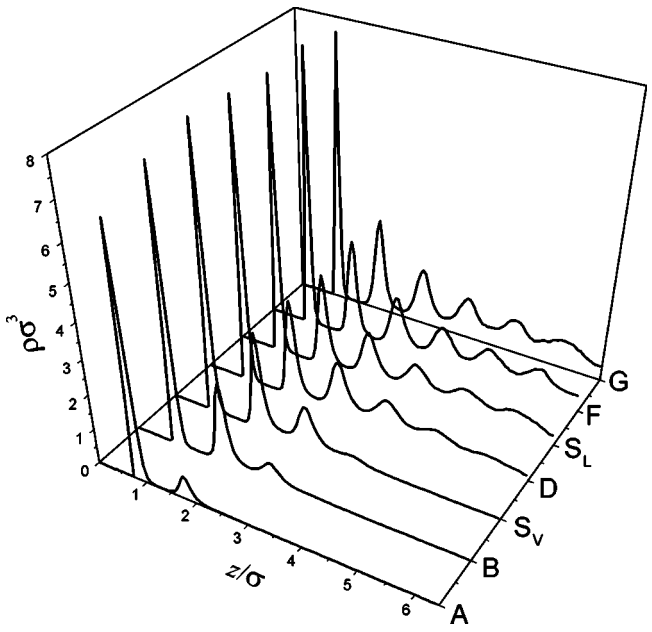

FIG. 3. Fluid density profiles in the 13σ pore at $kT/\epsilon=0.762$ (77.4 K). Different curves correspond to different states shown in Figs. 1 and 2(a). *A*, stable vaporlike state: *B*, vaporlike state at vapor-liquid coexistence: S_v, vaporlike spinodal: *D*, unstable state: S_l, liquidlike spinodal: *F*, liquidlike state at vapor-liquid coexistence: *G*, stable liquidlike state.

lated over the last 1.5×10^4 steps. Each GCMC step included a sequence of attempts of molecule displacement, insertion, and removal. In the GE simulations, each step included consequent attempts of molecule displacement in both cells and two attempts of molecule transfer from one cell the other.

B. GCMC and pore-gauge GEMC adsorption isotherms

Figures 2(a) and 2(b) show nitrogen adsorption-desorption isotherms in the pores of 13σ and 10σ in width. The GCMC adsorption isotherms exhibit typical features, such as the formation of a dense monolayer on the pore walls, followed by multilayer adsorption. We started the pore-gauge GEMC simulations from the densities, corresponding to the formation of the second layer. The density profile for pore 13σ pore in such a state is shown in Fig. 3 (line *A*). Good agreement between the GCMC and pore-gauge GEMC simulations was obtained for the multilayer films. In the 13σ pore at $\mu=-9.92\epsilon$ the GCMC isotherm underwent a spontaneous transition to a liquidlike state (capillary condensation). In the narrower 10σ pore, spontaneous condensation occurred at $\mu=-10.28\epsilon$ [Fig. 2(b)]. In the pore-gauge GEMC simulation, however, the number of molecules in the gauge cell was not sufficient for condensation in the pore cell. The formation of the multilayer film on the pore wall proceeded further in these simulations until the true limit of stability (vaporlike spinodal) was reached. Thus, in pore-gauge GEMC simulations the vaporlike spinodal is achievable, while in GCMC simulations the transition from a metastable vapor to a stable liquid occurs earlier when the free energy barrier between the two states is overcome by fluctuations.

The pore-gauge GEMC isotherm in the 13σ pore in the vicinity of the vaporlike spinodal is presented in Fig. 4. At this scale, the simulation points visibly scatter. However, the position of the spinodal can be determined quite precisely. We found that the data can be reasonably approximated by a parabola $\mu=\mu_{vs}+a(\rho-\rho_{vs})^2$ (Fig. 4). The quadratic correlation between μ and ρ in the vicinity of the spinodal point corresponds to the pseudocritical behavior at the spinodal, predicted by classical mean-field theories including local and nonlocal density functional theories (DFT) [47]. Unfortunately, it is not possible to draw a certain conclusion regarding the type of correlation between μ and ρ from our simulation, except to note that our results do not contradict the classical predictions (Fig. 4). From fitting the corresponding part of the isotherm by a parabola, we obtained $\mu_{vs}=-9.88\epsilon$, $\rho_{vs}=0.538\sigma^{-3}$ for the 13σ pore. In the vicinity of the spinodal point, the adsorbed film on the pore wall consisted of three pronounced layers (Fig. 3, line *C*).

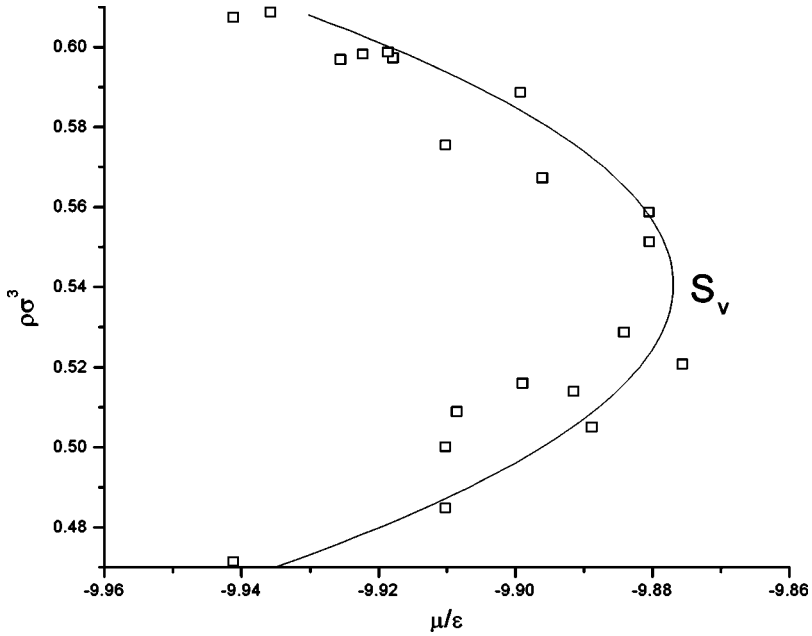

FIG. 4. Adsorption isotherm in the vicinity of the vaporlike spinodal (13σ pore at $kT/\epsilon=0.762$ is shown). The line shows the second-order polynomial fit $\mu=\mu_{vs}+a(\rho_{vs}-\rho)^2$.

Gradually increasing the density in the pore cell, we traced further thermodynamically unstable states between the vaporlike and liquidlike spinodals. Herewith, the chemical potential decreased monotonically with an increase in density. We obtained the location of the liquidlike spinodals S_l: $\mu_{sl}=-10.49\epsilon$, $\rho_{sl}=0.681\sigma^{-3}$ for the 13σ pore and $\mu_{sl}=-10.71\epsilon$, $\rho_{sl}=0.649\sigma^{-3}$ for the 10σ pore. The position of the liquidlike spinodal differs appreciably from point E of spontaneous desorption in the GCMC simulations, which is estimated by reducing the chemical potential from μ_* along the desorption branch of the adsorption isotherm (Fig. 2). The density profile in the liquidlike spinodal point for the 13σ pore is shown in Fig. 3, line S_l. As the density increases further, the pore-gauge GEMC isotherm smoothly merges with the desorption branch of the GCMC isotherm. In the stable liquidlike states, the adsorbate in the 13σ pore exhibits a distinct six-layer structure (Fig. 3, line H). Qualitatively simular GCMC and GEMC isotherms of nitrogen adsorption in carbon slit-shaped pores were constructed earlier [40].

C. Use of thermodynamic integration: Phase coexistence and the probability of spontaneous transitions

The changes of the grand thermodynamic potential along the S-shaped isotherm calculated by the integration of Eq. (5) are presented in Fig. 5. In order to compare the grand potentials obtained with the methods, we assumed that the stable equilibrium states determined by the GCMC and the pore-gauge GEMC methods are identical. This assumption does not influence the value of μ_e, obtained in the gauge cell method from the Maxwell rule. The equilibrium chemical potentials $\mu_e=-10.047\epsilon$ and -10.404ϵ were determined from the Maxwell rule for 13σ and 10σ pores, correspondingly. The vertical arrows indicate the limits of stability achieved in the GCMC simulations. At these points the potential associated with the transition from the metastable state to the stable state is rather small.

Figure 6 shows the Arrhenius factor P_*, Eq. (18), which determines the probability of spontaneous transitions from metastable to stable states in the hysteresis region. The transition probability equals 1 in the spinodal points and sharply decreases in their vicinities to vanishingly small values. In the 13σ pore, the reduction of the Arrhenius factor is as low as 10^{-25} at the equilibrium point, $\mu=\mu_e$ [inset in Fig. 6(a)]. In the narrower 10σ pore, the dependence is qualitatively similar: however, the reduction of the Arrhenius factor is substantially smaller. We expect that the Arrhenius factor strongly depends on the pore size. The squares in Fig. 6 show the locations of spontaneous capillary condensation and desorption transitions observed in the GCMC simulations. As expected, spontaneous transitions occurred close to the spinodals when the Arrhenius factor became nonvanishing. In real experiments, the level of fluctuations allowed is higher than in virtual experiments and, therefore, spontaneous transitions may occur closer to the equilibrium. This may explain the reversibility of the experimental isotherms of capillary condensation observed in pores narrower than ca. 40 Å where the simulated isotherms still exhibit prominent hysteresis [48]. A detailed discussion will be presented elsewhere.

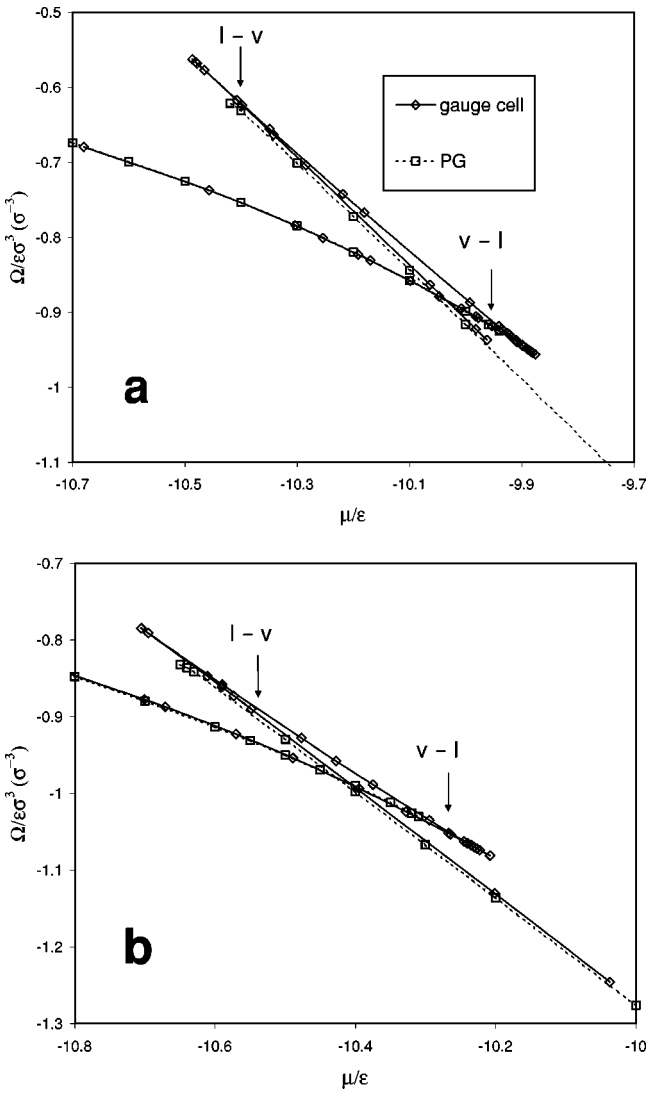

FIG. 5. Isotherms for the grand potential Ω at $kT/\epsilon=0.762$ (77.4 K) in the 13σ (a) and 10σ (b) pores calculated by the pore-gauge GEMC and PG methods ($\mu_*=-9.4\epsilon$ is shown). Arrows show the locations of spontaneous liquid-vapor and vapor-liquid transitions in the GCMC simulations.

V. COMPARISON WITH THE PG METHOD

In order to calculate phase coexistence by the PG method, supercritical isotherms at $kT/\epsilon=1.37$ (140 K) were generated with the GCMC method starting from $\mu_r=-22.0\epsilon$ to $\mu_*=-9.4\epsilon$, with an interval of $\Delta\mu=0.5\epsilon$. Here $\mu_r=-22\epsilon$ corresponds to the fluid density low enough to neglect fluid-fluid interactions in the pore. $\mu=-9.4\epsilon$ corresponds to a stable liquidlike state at $kT/\epsilon=0.762$ (77.4K) in both pores considered. The integration between the supercritical and subcritical adsorption isotherms was conducted at three different chemical potentials $\mu_*=-10.0$, -9.7, and -9.4ϵ; at each μ_*, GCMC simulations at five different temperatures $kT/\epsilon=1.3$, 1.18, 1.0, 0.93, and 0.85, were performed. The grand potentials for the adsorption branch $\Omega_a(\mu)$, calculated from GCMC and pore-gauge GEMC simulations practically coincide (Fig. 5). Due to uncertainty in the thermodynamic integration, $\Omega_d(\mu)$ for the desorption branch calculated from the PG method and the gauge cell method are somewhat shifted.

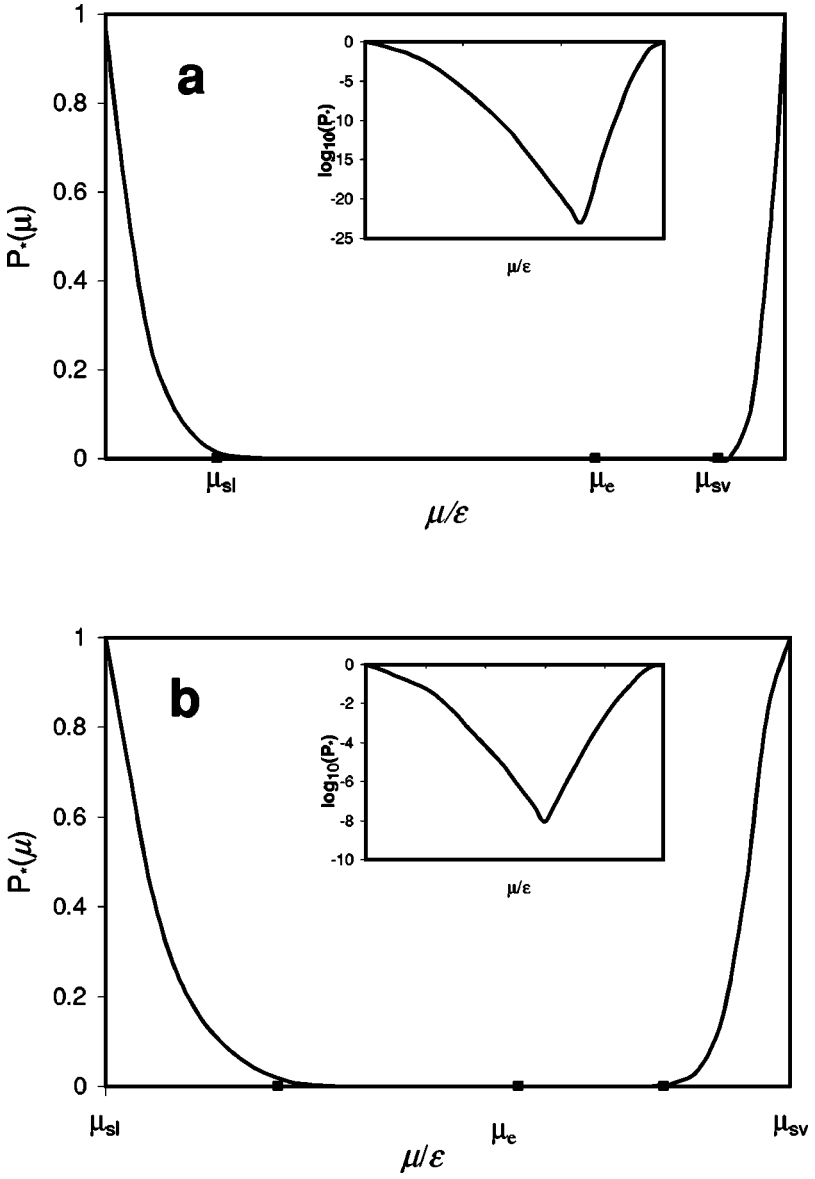

FIG. 6. The Arrhenius factor P_* for spontaneous transitions from the metastable to stable state in the 13σ (a) and 10σ (b) pores. P_* determines the probability of spontaneous capillary condensation at $\mu_e<\mu<\mu_{sv}$ and spontaneous capillary evaporation at $\mu_e<\mu<\mu_{sl}$. Squares show the locations of spontaneous transitions in the GCMC calculations. The depth of energy barriers is shown in inserts.

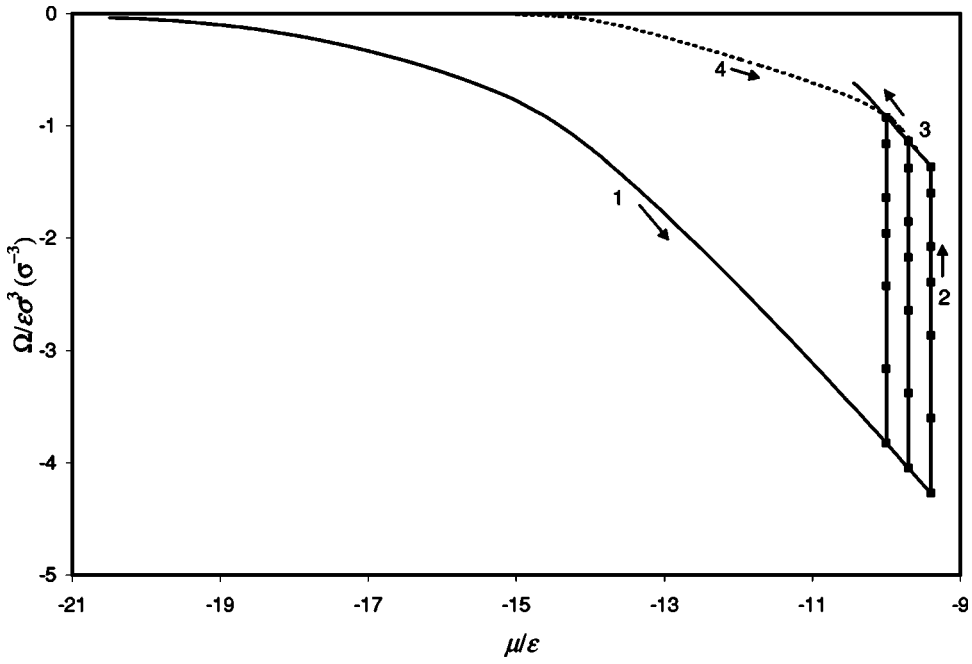

FIG. 7. Change of the grand potential along the reversible trajectories in the PG method in the 13σ pore. (1) Integration along the supercritical isotherm at $kT/\epsilon = 1.379$, (2) integration along path of constant chemical potential $\mu = \mu_*$ ($\mu_* = -10.0$, -9.7, and -9.4ϵ were used), (3) integration along the desorption isotherm (liquidlike states) at $kT/\epsilon = 0.762$, and (4) integration along the adsorption isotherm (vaporlike states) at $kT/\epsilon = 0.762$.

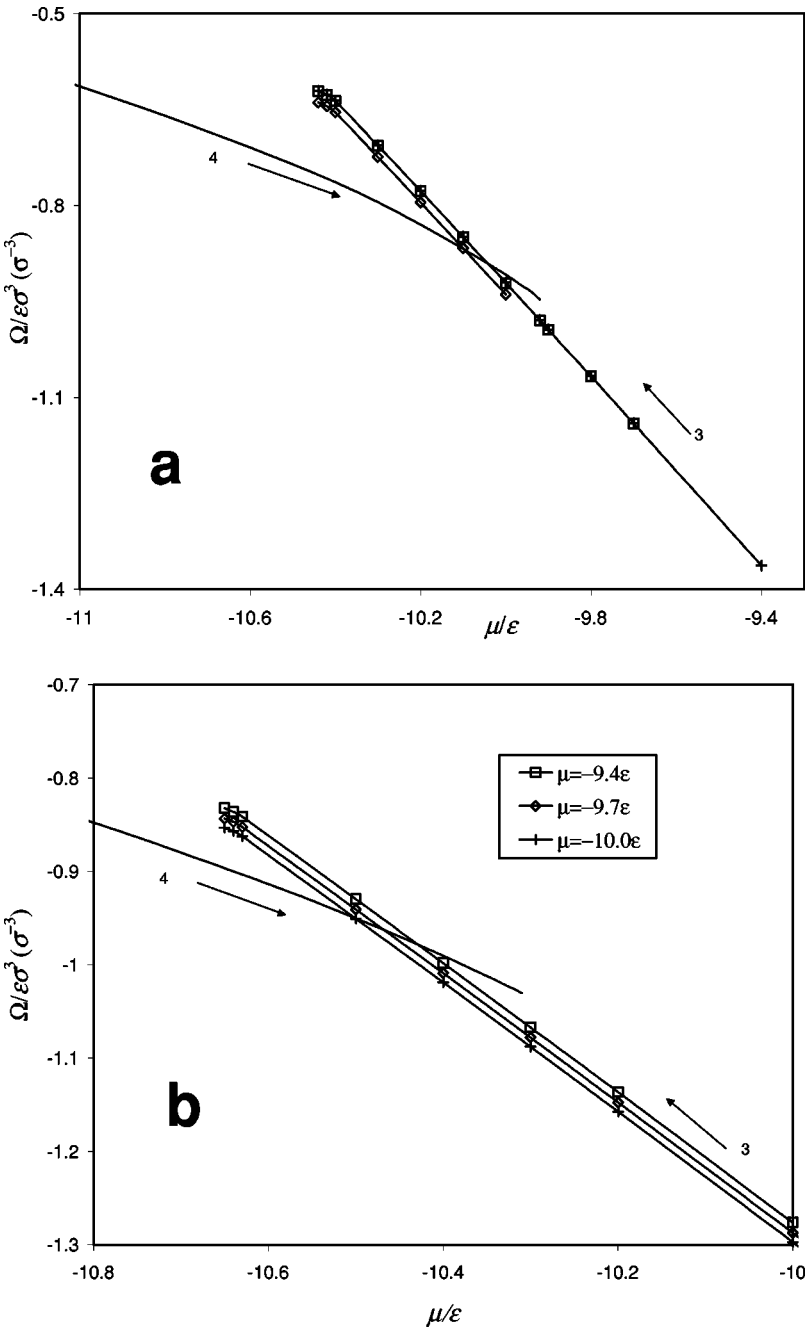

FIG. 8. Isotherms of the grand potential Ω at $kT/\epsilon=0.762$ (77.4 K) in the pores 13σ (a) and 10σ (b) calculated by the PG method along different reversible paths of equilibrium states (see Fig. 7).

For the 13ϵ pore, we have obtained good agreement between the results of the gauge cell method and PG method, for all three values of μ_* attempted. The values $\mu_e=-10.048$ and -10.041ϵ were obtained by the PG method with $\mu_*=-9.7$ and -9.4ϵ, respectively; $\mu_e=-10.047\epsilon$ ($P_e=0.4062$ atom) was obtained from integration along the unstable isotherm, indicating excellent agreement between the two methods. The isotherm for $\Omega_d(\mu)$ obtained from the PG method with $\mu_*=-10.0\epsilon$ lies $0.017\epsilon\sigma^{-3}$ lower, resulting in $\mu_e=-10.064\epsilon$ ($P_e=0.3819$), which is an appreciable difference with respect to some practical applications, such as pore structure characterization of nanoporous materials [26,46]. The equilibrium μ_e, averaged over the three μ_*, and μ_e from the gauge cell method are shown in Fig. 2.

A similar situation was observed for the 10σ pore [Figs. 2(b) and 5(b)]. The GCMC and pore-gauge GE simulation data agree well. At the same time, appreciable scattering of μ_e calculated by the PG method was found: $\mu_e=-10.395$, -10.417, and -10.431ϵ were calculated using different routes of integration with $\mu=-9.7$, -9.7, and -10.0ϵ, respectively. These discrepancies reflect the numerical instability of the PG thermodynamic integration.

Figure 7 shows different contributions to the total grand potential of the confined fluid in the 13σ pore. Integration along the supercritical adsorption isotherm $T_s=1.379$ from the reference point $\mu_{rs}=-22\epsilon$ to $\mu_*=-9.7\epsilon$ (stage 1) yielded $\Omega_s(\mu_*)=-4.27\epsilon\sigma^{-3}$. After integration along the path of constant chemical potential (stage 2), we obtained $\Omega_d(\mu_*)=-1.36\epsilon\sigma^{-3}$. Due to a large compensation, an error of only 0.4% in integration along the supercritical isotherm and/or along the path of constant chemical potential corresponds to the shift of 0.05ϵ in μ_e for this pore. The numerical instability of the PG method is demonstrated in Fig. 8, which shows $\Omega_d(\mu)$ obtained with three different

values of μ_* and $\omega_a(\mu)$ for both pores. The differences in $\Omega_d(\mu)$ obtained by integration with three different μ_* resulted in a substantial deviation in μ_e, especially for the 10σ pore. However, at the scale of Fig. 8 these differences are practically indistinguishable. In contrast to the PG method, thermodynamic integration along the S-shaped adsorption isotherm deals with contributions of the same order of magnitude and, thus, is expected to be more stable with respect to possible simulation errors.

VI. COMPARISON WITH THE PORE-PORE GEMC METHOD

We also applied the pore-pore GEMC simulation technique [22] to estimate the vapor-liquid coexistence in the pores. We made one attempt at volume exchange per 50 steps (each step included one attempt at molecule displacement in both cells and two attempts at molecule transfer between the cells). The magnitude of the volume change was adjusted automatically so that every second attempt at volume transfer was successful. The total length of the pore-pore GEMC simulations was 3×10^7 steps. In order to test the algorithm, we repeated the simulations from the original work of Panagiotopoulos [22] of the densities of the coexisting liquid and vapor argon in the cylindrical pore of solid CO_2 with $H=8\sigma$ at $kT/\epsilon=0.7$ and found satisfactory agreement. It is worth noting that due to a weak adsorption field imposed on argon by pore walls made of solid CO_2 (it is less than half as strong as the adsorption field of the silica walls), the dense adsorbed monolayer of argon is not observed. This makes the pore-pore GEMC simulations as efficient as those in bulk systems. On the contrary, nitrogen adsorbed in silica pores forms a dense (two-dimensional crystal-like) hexatic adsorbed monolayer in both vaporlike and liquidlike states in the hysteresis region. In this case, the mechanical equilibrium may be significantly hindered.

The sensitivity of the pore-pore GEMC method with respect to the choice of configuration was tested by employing different sets of initial configurations. The initial configurations in the vapor and liquid cells were taken from GCMC simulations of the vaporlike and liquidlike states. The length of both cells in the initial configuration was set to 10σ. For the 13σ pore, one set of initial configurations corresponded to the liquidlike and vaporlike states at $\mu=-10.4\epsilon$, close to the liquidlike spinodal; another one was chosen at $\mu=-9.96\epsilon$, close to the vaporlike spinodal. Thus, these initial states were at chemical equilibrium but far from mechanical equilibrium. We found that the results of pore-pore GEMC simulations depend dramatically on the initial configuration. The equilibrium densities of the vaporlike and liquidlike phases fitted well the isotherms obtained by the GCMC and gauge cell methods. However, when interpolated, the vapor density yielded unrealistic values of μ_e. For example, $\mu_e=-10.18\epsilon$ and -9.98ϵ were obtained when simulations started from vaporlike and liquidlike configurations at $\mu=-10.4$ and -9.98ϵ, respectively.

For the narrower pore of 10σ in width, the influence of the initial configuration was found to be even more pronounced. In this pore, we used three different sets of initial configurations: liquidlike and vaporlike states at $\mu=-10.5\epsilon$ (close to the liquidlike spinodal) and $\mu=-10.3\epsilon$ (close to the liquidlike spinodal) and a pair of states, which were not in chemical equilibrium, the liquidlike state at $\mu=-9.7\epsilon$ and vaporlike state at $\mu=-10.5\epsilon$. However, in none of the simulations did the volumes of the cells show a deviation from the initial value larger than 3%, and the resulting densities depended on the initial configuration. This means that equilibrium in the pore-pore GEMC simulations was not reached.

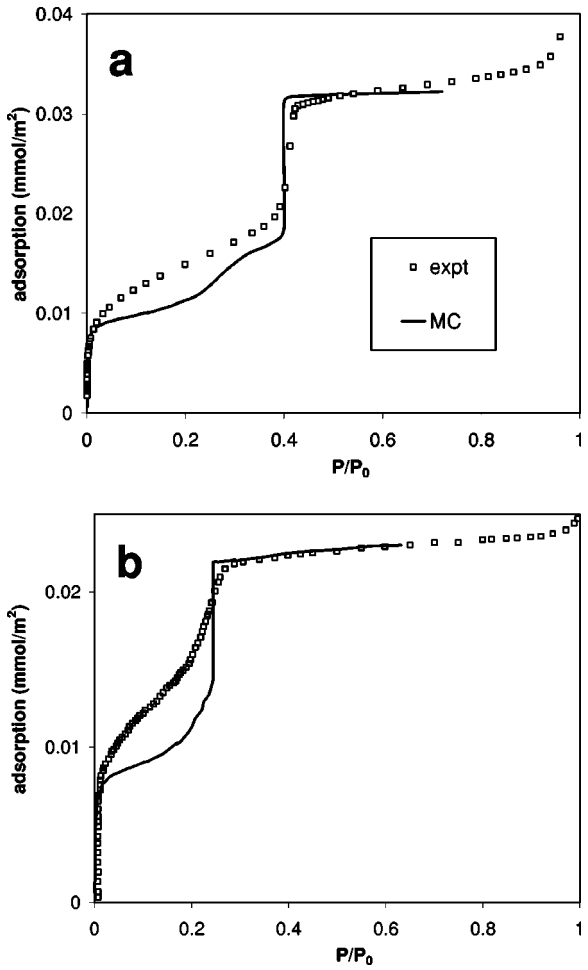

FIG. 9. Comparison of the calculated capillary condensation isotherms with experimental desorption isotherms on MCM-41 materials at 77.4 K [3,6]. (a) 13σ pore (internal diameter 44.2 Å), and (b) 10σ pore (internal diameter 35.5 Å).

VII. COMPARISON WITH EXPERIMENT

In Fig. 9 we compare the simulated equilibrium isotherms in the 13σ and 12σ cylindrical pores with the experimental desorption isotherms on the samples of MCM-41 mesoporous molecular sieves. MCM-41 materials presumably contain uniform arrays of cylindrical pores of predetermined diameter and are the best available reference materials for adsorption studies [3,49]. The samples used for comparison were chosen from the literature [3,5] since they have relatively narrow pore size distributions around 33.4 and 44.5 Å, in correspondence with the widths of cylinders employed in simulations. The pore size distributions were estimated by the DFT method [49]. The experimental isotherm in the 33.4 Å sample was reversible, while the isotherm in the 44.5 Å

sample exhibited a small hysteresis. In this case, we used the desorption branch which, in the case of open-ended cylindrical channels of MCM-41 materials, is assumed to be close to the line of equilibrium transitions [48].

We see that the capillary condensation step on the experimental isotherms is rounded, as expected for a phase transition in a system composed of a large number of finite size pores with inevitable variations in pore width. Note that the simulated isotherms differ significantly from the experimental in the region of adsorption prior to capillary condensation. This deviation is likely caused by the energetic heterogeneity inherent in silica surfaces [50]. However, the inflection point on the capillary condensation step agrees with the position of the theoretical phase transition in the pore of mean size predicted by the gauge cell method. For the narrower pore of the 10σ pore, the position of phase coexistence was calculated as $P_e/P_0=0.245$ versus the value $P_e/P_0=0.237$ estimated from the experimental isotherm. For the wider 13σ pore, the respective theoretical and experimental values are 0.401 and 0.408. These deviations are quite small and indicate good agreement of the predicted phase equilibrium with the experimental results.

VIII. CONCLUSION

An efficient alternate method for Monte Carlo studies of phase equilibrium in confined systems is presented using the example of vapor-liquid equilibrium (capillary condensation and evaporation) in pores. The method is based on the construction of the full phase diagram of a confined fluid in the form of a van der Waals loop, which includes stable, metastable, and unstable equilibrium states. The phase coexistence is then determined by thermodynamic integration along the metastable and unstable regions of the phase diagram, employing Maxwell's rule of equal areas. The phase diagram of a fluid within a given pore is obtained by the Gibbs ensemble Monte Carlo simulation of the equilibrium distribution of molecules between two simulation cells, one of which represents the pore and the other one a gauge cell. The phase diagram of the fluid in the gauge cell is assumed to be known. The gauge cell method allows one to determine the equilibrium transition as well as the true limits of stability of vaporlike and liquidlike metastable states or the vaporlike and liquidlike spinodals. It is shown that in the vicinity of the spinodal the system exhibits pseudocritical behavior. The spinodals determined by the gauge cell method are shown to differ from the points of spontaneous condensation and evaporation in the GCMC simulations. A method is suggested for calculating the energy barriers between the metastable and stable states. The height of the energy barrier is determined by the grand potential in the saddle point that corresponds to an unstable state on the backward trajectory of the phase diagram. The calculated potential barriers and corresponding Arrhenius factors for the transition between the metastable and stable states determine the conditions of spontaneous condensation and evaporation. It is shown that spontaneous transitions, observed in the GCMC simulations, occurred close to the spinodals when the Arrhenius factor became nonvanishing. The results of the gauge method for the phase coexistence were compared with the methods of the thermodynamic integration of Peterson and Gubbins and the pore-pore GEMC simulation of Panagiotopoulos, proposed earlier, and also with the experimental data on the capillary condensation of nitrogen at its boiling temperature in cylindrical pores of mesoporous molecular sieves. The gauge cell method gives a useful insight into the vapor-liquid coexistence and origin of the capillary hysteresis inherent in nanoporous materials. The method can also be applied to other phase transitions in confined systems such as fluid-fluid separation, layering and freezing.

ACKNOWLEDGMENTS

The authors thank Peter Ravikovitch for fruitful discussions. This work was supported by the TRI/Princeton exploratory research program and EPA Grant No. R825959-010.

[1] L. D. Gelb, K. E. Gubbins, R. Radhakrishnan, and M. Sliwinska-Bartkowiak, Rep. Prog. Phys. **62**, 1573 (1999).
[2] S. J. Gregg and K. S. W. Sing, *Adsorption, Surface Area and Porosity* (Academic Press, London, 1982).
[3] P. I. Ravikovitch, S. C. O'Domhnaill, A. V. Neimark, F. Schuth, and K. K. Unger, Langmuir **11**, 4765 (1995).
[4] A. V. Neimark, P. I. Ravikovitch, M. Grün, F. Schüth, and K. K. Unger, J. Colloid Interface Sci. **207**, 159 (1998).
[5] K. Morishige and M. Shikimi, J. Chem. Phys. **108**, 7821 (1998).
[6] M. Kruk, M. Jaroniec, and A. Sayari, J. Phys. Chem. B **101**, 583 (1997).
[7] Q. Huo, D. I. Margoles, and G. D. Stucky, Chem. Mater. **8**, 1147 (1996).
[8] B. K. Peterson, K. E. Gubbins, G. S. Heffelfinger, U. M. B. Marconi, and F. van Swol, J. Chem. Phys. **88**, 6487 (1988).
[9] E. I. Segarra and E. D. Glandt, Chem. Eng. Sci. **49**, 2953 (1994).
[10] W. Gac, A. Patrykiejew, and S. Sokolowski, Surf. Sci. **306**, 434 (1994).
[11] S. Jiang, C. L. Rhykerd, and K. E. Gubbins, Mol. Phys. **89**, 373 (1993).
[12] E. N. Brodskaya and E. M. Piotrovskaya, Langmuir **10**, 1837 (1994).
[13] S. Samios, A. K. Stubos, N. K. Kanellopoulos, R. F. Cracknell, G. K. Papadopoulos, and D. Nicholson, Langmuir **13**, 2795 (1997).
[14] M. J. Bojan and M. J. Steele, Carbon **36**, 1417 (1998).
[15] A. Vishnyakov, E. M. Piotrovskaya, and E. N. Brodskaya, Adsorption **4**, 207 (1998).
[16] N. B. Wilding and M. Schoen, Phys. Rev. E **60**, 1081 (1999).
[17] L. D. Gelb and K. E. Gubbins, Langmuir **15**, 305 (1999).
[18] B. K. Peterson and K. E. Gubbins, Mol. Phys. **62**, 215 (1987).
[19] M. Miyahara, T. Yoshioka, and M. Okazaki, J. Chem. Phys. **106**, 8124 (1997).
[20] J. Forsman and C. E. Woodward, Mol. Phys. **96**, 189 (1997).
[21] A. Z. Panagiotopoulos, Mol. Phys. **61**, 813 (1987).
[22] A. Z. Panagiotopoulos, Mol. Phys. **62**, 701 (1987).
[23] K. Johnson, J. A. Zollweg, and K. E. Gubbins, Mol. Phys. **78**, 591 (1993).

[24] B. Widom, J. Chem. Phys. **39**, 2808 (1963).
[25] B. Smit, J. Chem. Phys. **96**, 8639 (1992).
[26] C. M. Lastoskie, N. Quirke, and K. E. Gubbins, Stud. Surf. Sci. Catal. **104**, 745 (1997).
[27] A. Vishnyakov, E. M. Piotrovskaya, E. N. Brodskaya, E. V. Votyakov, and Yu. K. Tovbin, Rus. J. Phys. Chem. **74**, 162 (2000).
[28] W. T. Gozdz, K. E. Gubbins, and A. Z. Panagiotopoulos, Mol. Phys. **84**, 825 (1995).
[29] A. M. Ferrenberg and R. H. Swendsen, Phys. Rev. Lett. **61**, 2635 (1988).
[30] A. M. Ferrenberg and R. H. Swendsen, Phys. Rev. Lett. **63**, 1195 (1989).
[31] L. D. Gelb and K. E. Gubbins, Phys. Rev. E **55**, R1290 (1997).
[32] D. A. Kofke, Adv. Chem. Phys. **105**, 405 (1999).
[33] J.-P. Hansen and L. Verlet, Phys. Rev. **184**, 151 (1969).
[34] D. H. Everett, in *The Solid-Gas Interface*, edited by E. A. Flood (Marcel Decker, New York, 1967), Vol. 2, p. 1055.
[35] R. Evans, U. M. B. Marconi, and P. Tarazona, J. Chem. Phys. **84**, 2376 (1986).
[36] P. C. Ball and R. Evans, Langmuir **5**, 714 (1989).
[37] D. Nicholson, J. Chem. Soc., Faraday Trans. 1 **71**, 239 (1975).
[38] G. L. Aranovich and M. D. Donohue, Phys. Rev. E **60**, 5552 (1999).
[39] A. de Keizer, Th. Michalski, and G. H. Findenegg, Pure Appl. Chem. **10**, 1495 (1991).
[40] V. Yu. Gusev, in *Microscopic Simulations of Interfacial Phenomena in Solids and Liquids*, edited by P. Bristowe, S. Phillpot, J. Smith, and D. Stroud, MRS Symposia Proceedings Series No. **492**, (Materials Research Society, Pittsburgh, 1998), p. 35.
[41] A. V. Neimark and P. I. Ravikovitch, in *Microscopic Simulations of Interfacial Phenomena in Solids and Liquids* [40], p. 27; A. V. Niemark and P. I. Ravikovitch, Stud. Surf. Sci. Catal. **128**, 51 (2000).
[42] S. C. McGrother and K. E. Gubbins, Mol. Phys. **97**, 955 (1999).
[43] D. H. Everett, Colloids Surf., A **141**, 297 (1998).
[44] A. Gonzalez, J. A. White, F. L. Roman, S. Velasco, and R. Evans, Phys. Rev. Lett. **79**, 2466 (1997).
[45] A. V. Neimark and P. I. Ravikovitch (unpublished).
[46] P. I. Ravikovitch, A. Vishnyakov, R. Russo, and A. V. Neimark, Langmuir **16**, 4648 (2000).
[47] A. Compagner, Physica (Amsterdam) **72**, 115 (1974).
[48] A. V. Neimark, P. I. Ravikovitch, and A. Vishnyakov, Phys. Rev. E **62**, 1493 (2000).
[49] P. I. Ravikovitch, D. Wei, W. T. Chueh, and A. V. Neimark, J. Phys. Chem. **101**, 3671 (1997); A. V. Neimark. P. I. Ravikovitch, M. Grün, F. Schüth, and K. K. Unger, J. Colloid. Interface Sci. **207**, 159 (1998); P. I. Ravikovitch, G. L. Haller, and A. V. Neimark, Adv. Colloid. Interface Sci. **76-77**, 203 (1998); P. I. Ravikovitch, S. C. O'Domhnaill, A. V. Neimark, F. Schüth, and K. K. Unger, Langmuir **11,** 4765 (1995).
[50] M. W. Maddox, J. P. Olivier, and K. E. Gubbins, Langmuir **13**, 1737 (1997).